JAMES | Journal of Advances in Modeling Earth Systems

RESEARCH ARTICLE
10.1029/2019MS001793

This article is a companion to Coppin & Bellon (2019) https://doi.org/10.1029/2019MS001794.

Key Points:
- Systematic offshore propagation of convection is observed at night, with varying distance of propagation
- Offshore convection triggered by gravity waves modulates the propagation speed of the land breeze
- Large-scale environment controls propagation with a dry and warm anomaly at the top of the boundary layer

Correspondence to:
D. Coppin,
david.ad.coppin@gmail.com

Citation:
Coppin, D., & Bellon, G. (2019). Physical mechanisms controlling the offshore propagation of convection in the tropics: 1. Flat island. *Journal of Advances in Modeling Earth Systems*, *11*, 3042–3056. https://doi.org/10.1029/2019MS001793

Received 28 JUN 2019
Accepted 31 AUG 2019
Accepted article online 6 SEP 2019
Published online 13 SEP 2019

©2019. The Authors.
This is an open access article under the terms of the Creative Commons Attribution License, which permits use, distribution and reproduction in any medium, provided the original work is properly cited.

Physical Mechanisms Controlling the Offshore Propagation of Convection in the Tropics: 1. Flat Island

David Coppin[1] **and Gilles Bellon**[1]

[1]Department of Physics, University of Auckland, Auckland, New Zealand

Abstract An idealized convection-permitting simulation is performed to investigate the physical mechanisms responsible for the nighttime offshore propagation of convection around tropical islands. An idealized island is placed in the middle of a long, nonrotating channel oceanic domain with constant sea surface temperature. A strong diurnal cycle typical of a tropical island is simulated, with a thermally forced sea breeze in daytime and the associated inland propagation of precipitation. Offshore propagation of a land breeze and its associated convection is simulated every night but with varying extent. Gravity waves of first and second baroclinic modes trigger convection far from the coast if the offshore conditions are favorable. This accelerates the propagation speed of the land breeze as it reduces the onshore wind associated with the lower branch of the overturning large-scale circulation. Higher-order modes may trigger convection or reinforce existing convection but less systematically. The distance of propagation is particularly sensitive to humidity and temperature at the top of the boundary layer, with occasional incursions of a dry anomaly at the top of the boundary layer near the island preventing convection from developing far from the island.

Plain Language Summary Climate models have problems modeling the precipitation pattern, timing, and atmospheric circulation associated with tropical island regions. This impacts the prediction of planetary scale events such as the Madden-Julian Oscillation. Part of this problem originates from the poor representation of islands and their topography, which affects the diurnal cycle of convection over land and the surrounding oceans. This diurnal cycle generates a sea breeze during daytime, which triggers convection over the island in the afternoon, early evening. At night, the breeze reverses and becomes a land breeze that propagates over the ocean. In order to understand what controls this offshore propagation, we study the movement of convection around an idealized tropical island. We show that a land breeze is systematically present even though its distance of propagation depends on the presence of offshore convection triggered by gravity waves earlier and on the humidity and temperature between 1 and 2 km of altitude close to coast. Properly modeling these individual elements may improve the precipitation pattern and atmospheric circulation around tropical islands and be beneficial for improving the representation of atmospheric phenomenons impacted by these regions.

1. Introduction

Islands are focal points for the development of convection in the tropics. If they are sufficiently far from the continent and sufficiently large, they can be seen as a fixed and localized forcing in the middle of a uniform ocean (Sobel et al., 2011). This forcing primarily comes from the lower heat capacity of land relative to ocean. The solar forcing on these two contrasted surfaces results in a sea breeze circulation during the day when land warms rapidly and winds blow toward the island, followed by a smaller land breeze in the opposite direction at night (Mori et al., 2004; Qian, 2008).

This land-sea breeze circulation controls the diurnal cycle (DC) of convection and precipitation over and around tropical islands. This diurnal cycle is characterized by a concentration of clouds and precipitation over land during daytime, with a peak in the early evening, and over sea at night, with a maximum in early morning (e.g., Yang & Slingo, 2001; Nesbitt & Zipser, 2003; Mori et al., 2004). Mountain ranges, and the upslope winds they generate in the afternoon, enhance precipitation over the islands (Mapes et al., 2003; Qian, 2008; Sobel et al., 2011; Yang & Slingo, 2001). This is particularly true over the main islands of the Maritime Continent: Sumatra (Mori et al., 2004; Yokoi et al., 2017), Borneo (Ichikawa & Yasunari, 2007; Qian

et al., 2013), and New Guinea (Hassim et al., 2016; Ichikawa & Yasunari, 2008; Vincent & Lane, 2016). The land breeze at night is responsible for an offshore propagation of coastal convection over the surrounding ocean (Hassim et al., 2016; Li et al., 2017; Love et al., 2011; Mori et al., 2004; Qian, 2008; Saito et al., 2001; Vincent & Lane, 2016).

Most general circulation models (GCMs) fail to reproduce the diurnal cycle of convection over the Maritime Continent properly, which results in large systematic precipitation errors (Neale & Slingo, 2003; Qian, 2008). Part of this problem stems from the poor horizontal resolution and the underrepresentation, or absence, of islands and mountains, thus weakening the atmospheric disturbances caused by the diurnal cycle. More recent GCMs with horizontal resolution down to (1/3)° still have issues simulating the timing and amplitude of the diurnal cycle (e.g., Peatman et al., 2015). The correct representation of the delayed increase in cloudiness and precipitation relative to the solar heating is also a significant problem in most GCMs, even though some new parameterizations have made progress toward solving this issue (Rochetin et al., 2014; Bechtold et al., 2014). More realistic timing and amplitude of precipitation can also be simulated when horizontal resolution is increased sufficiently to resolve cloud systems (grid spacing of 5 km or finer; Sato et al., 2009; Love et al., 2011).

In order to improve the timing and amplitude of the diurnal cycle in GCMs, it is important to understand the physical mechanisms controlling the land-sea breeze circulations and how they interact with the large-scale environment. One approach is to identify key features missing in coarse-resolution simulations in order to parameterize their effect. In the present study, we attempt to understand the mechanisms of the nocturnal offshore propagation. The extent of the observed propagation is quite surprising (Love et al., 2011), far from the thermal contrast that first caused the land breeze. By comparison, the daytime propagation of the sea breeze rarely penetrates beyond 100 km inland.

Gravity waves have long been hypothesized as important contributors to the offshore propagation of convection (Mapes & Houze, 1993; Mapes et al., 2003). Several studies have identified different propagation speeds of convection and related them to gravity waves. In observations, Mori et al. (2004) found an averaged front propagation at 10 m/s within 400 km from the coast, slower than the 15–20 m/s from Mapes et al. (2003) but faster than the 8 m/s estimated by Yokoi et al. (2017). The precipitation maximum propagates at a more reduced speed between 3 and 5 m/s (Mori et al., 2011; Yokoi et al., 2017). Modeling work also shows some variability in the propagation speed. In their most realistic simulation of the diurnal cycle, Love et al. (2011) identified a first internal gravity wave which is excited in early afternoon and propagates at 40 m/s. But precipitation follows the offshore propagation (3–5 m/s) of a higher-order gravity wave mode triggered by a change of heating profile due to stratiform convection in the mid-afternoon. Hassim et al. (2016) found gravity waves propagating at 15 m/s similar to Mapes et al. (2003) even though they do not trigger convection. On the other hand, they make the environment more conducive to deep convection and likely contribute to the longevity of squall lines propagating at 5 m/s. They also mention that the offshore rainfall onset propagates at 8 m/s. Using the same model, Vincent and Lane (2016) emphasize that land-valley breezes persisted for 100–200 km offshore and moved with a speed of 3–5 m/s too, while farther offshore, faster bands of convection moved at 12–18 m/s.

These results, even though they seem to lead in the same direction, emphasize how difficult it is to generalize results from observations and realistic modeling studies which are sensitive to many factors such as large-scale humidity or background wind. Because they can partially control such factors, idealized simulations prove useful to clearly identify mechanisms. Tulich and Mapes (2007) looked at multiscale convective wave disturbances emerging from a two-dimensional cloud model forced by uniform cooling over a uniform ocean. They showed that upper-level convective heating excites waves packets moving at 16–18 m/s over the ocean, while gust front wave packets excited by cooling over the boundary layer propagate at 8 m/s and trigger new convection in the vicinity of earlier convection. Cronin et al. (2015) used such idealized simulations to investigate the island precipitation enhancement. They attributed the island enhancement to a mechanism of rectification of the diurnal cycle which, they found, is sensitive to island size. Wang and Sobel (2017) also used idealized simulations to investigate the role of the mean wind and found that for large wind, the mechanism of diurnal cycle rectification is ineffective because horizontal transport of temperature reduces the land-sea thermal contrast that drives the sea breeze. Instead, they found that fast winds create mechanically forced convergence and precipitation.

The aim of this study is to characterize the physical mechanisms responsible for the nocturnal offshore propagation of convection around an idealized island. The dependence of these mechanisms on topography will be investigated in a companion paper. Section 2 describes the model and setup of the simulations. Section 3 presents the global characteristics of the simulation. Section 4 analyzes offshore convective propagation as a function of maximum distance of propagation. Sections 5 and 6 focus on the land breeze front and the gravity waves that control the triggering of offshore convection. Section 7 investigates the control of the distance of propagation by the large-scale environment.

2. Methods

We use the mesoscale nonhydrostatic atmospheric model Meso-NH version 5.3.1 (Lafore et al., 1998; Lac et al., 2018), developed jointly by the Laboratoire d'Aérologie and the Centre National des Recherche Météorologiques. Cloud microphysical processes are represented by the ICE3 scheme (Pinty & Jabouille, 1998) that includes six different types of hydrometeors. The turbulence is solved by a three-dimensional scheme using a prognostic equation for the turbulent kinetic energy (Cuxart et al., 2000) with the turbulent mixing length given by the mesh size. The scheme of Pergaud et al. (2009) is used to represent dry thermals in the atmospheric boundary layer and to parameterize the effects of unresolved shallow convective clouds. Longwave radiation calculation is done using RRTM scheme: Morcrette, (1991, 2002), while the shortwave radiation calculations are based on Fouquart and Bonnel (1980). Surface processes and interactions with the atmosphere are simulated by the SURFEX model (Masson et al., 2013) coupled with Meso-NH.

In our simulation, the domain is a long doubly periodic channel, 2,048 km × 128 km in x and y directions, respectively, with 47 stretched vertical levels and a top at 25 km. The horizontal grid spacing is 4 km. There is no large-scale wind. A flat island of 128 km × 128 km is placed in the middle of the domain. This width corresponds to the typical width of medium-large tropical islands such as Java. Doubling it or dividing it by 3 encompass the vast majority of tropical islands with a distinct diurnal cycle. With this width, we also allow the spatial scales for variability over the island to be the same in the x and y directions. The model is run in Radiative-Convective Equilibrium (RCE) configuration without rotation. RCE is the statistical equilibrium state the atmosphere and surface would reach in the absence of lateral energy transport (Emanuel et al., 2014). This framework is widely used to understand the basic properties of the tropical atmosphere. It has been applied successfully to tropical islands (Cronin et al., 2015; Wang & Sobel, 2017). Diffusion and damping are used in the top levels to prevent unrealistic momentum transport. We also apply damping on the first and last 80 km of the periodic x direction to avoid gravity wave propagation from one side of the domain to the other.

The sea surface temperature (SST) is fixed at 301 K, a typical deep-tropics SST. A novel aspect of our configuration is the use of the state-of-the-art SURFEX land model that includes a soil-vegetation scheme (ISBA; Noilhan and Planton (1989)). In our setup, 80% of the island is covered by evergreen broadleaf trees, the rest by bare land. The evergreen broadleaf trees is the vegetation type used to characterize tropical vegetation in land models. In order to get a realistic heat capacity of the soil in our model, we set the bare land proportion to 20%, larger than observed values (5%). The near-infrared, visible, and ultraviolet albedos of bare land are set to 0.25 and those of the evergreen broadleaf vegetation to 0.12. In order to simulate reasonable oceanic surface fluxes and to avoid spurious effects from the contrast between the fixed-SST ocean, which acts as an energy sink, and the island, which has a zero net long-term surface heat flux, we follow the approach of Cronin et al. (2015) and reduce the insolation at the equator by one quarter. This leads to a time-mean insolation of 330 W/m^2, with the sun rising at 06:00, a top-of-atmosphere maximum insolation of 1,035 W/m^2 at 12:00 and the Sun setting at 18:00 everywhere at the same time.

We initialize the simulation with the mean vertical profile of a RCE simulation with the same SST over a 300-km × 300-km domain at 3-km resolution. A white noise of 0.1 K (maximum at 30 m) is added to the first five levels to initiate subdomain variability. The simulation lasts 250 days. We analyze the last 200 days, for which the model reached a stationary state.

The budget equations for momentum, temperature, and water vapor are calculated directly in flux form by the model, which stores the changes in each variable after exiting the corresponding routine. The resulting budget provides useful information that enables us to investigate the physical mechanisms at play (e.g., Cuxart et al., 2014). Here, we use 1-hr averages for the 200 days studied and each grid point. The three budgets are given by the following equations:

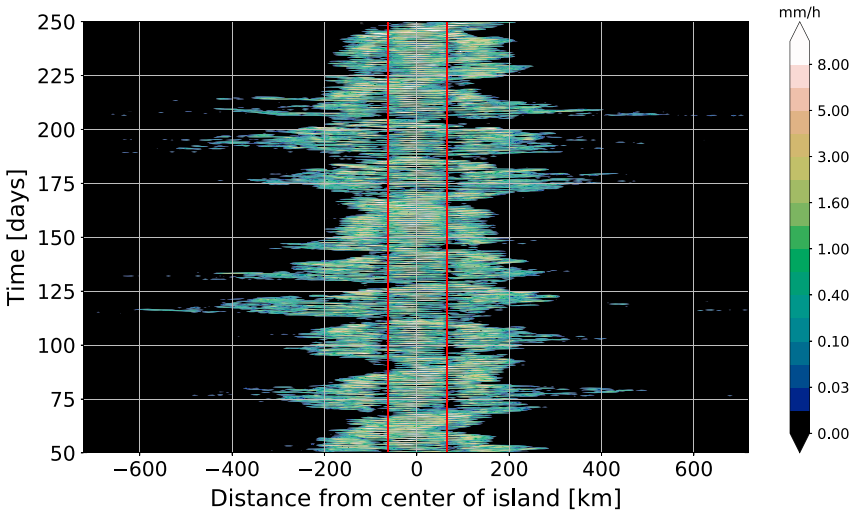

Figure 1. Hovmoller plot of precipitation for the 200 days considered. Precipitation is averaged in the *y* direction for every time step. The red lines show the coasts of the island.

$$\frac{\partial U_i}{\partial t} = -U_j \frac{\partial U_i}{\partial x_j} - \frac{1}{\rho}\frac{\partial p}{\partial x_j} + \delta_i g \frac{\Delta \Theta_v}{\Theta_{vref}} - \frac{\partial \overline{U_j' U_i'}}{\partial x_j} + \text{ShConv} + \text{Diff} \tag{1}$$

$$\frac{\partial T}{\partial t} = -U_j \frac{\partial T}{\partial x_j} - \frac{1}{\rho}\frac{\partial R_j}{\partial x_j} - \frac{\partial \overline{U_j' T'}}{\partial x_j} + \text{PC} + \text{ShConv} - \text{Diss} \tag{2}$$

$$\frac{\partial q}{\partial t} = -U_j \frac{\partial q}{\partial x_j} - \frac{\partial \overline{U_j' q}}{\partial x_j} + \text{PC} + \text{ShConv} \tag{3}$$

In the momentum budget, equation (1), Diff is the diffusion term and ShConv the term related to unresolved shallow convective clouds. In the temperature equation, equation (2), R_j is the net radiative flux in direction j. PC corresponds to the sources and sinks related to phase changes and Diss to molecular dissipation. The humidity equation, equation (3), has the same terms except for the radiative and dissipation terms. In our simulation, the advective term (first term on the right-hand side in all equations) is calculated as the sum of all directions. Diff and Diss being very small, they will not be shown in our figures. Rain evaporation will be isolated from the other phase changes to show its specific effect on the different variables.

3. Global Composites

In the following sections, we present in detail the flat island simulation and the mechanisms controlling its offshore propagation of convection. Except in Figures 1 and 5, all the figures show the center of the island on the left and the distance is measured from the coast, positive offshore.

In this simulation, precipitation occurs daily over the island (Figure 1), propagating inland from midday to the evening and subsequently propagates offshore. Considering the simplicity of our setup, these results show how fundamental this propagation is. The propagation is roughly symmetric about the center of the island. Compositing for all days and both sides of the island shows that precipitation over the island is maximum between 18:00 and 21:00 and rarely lasts after 06:00 (Figure 2). On the other hand, precipitation is maximum over the ocean from 00:00 to 09:00 and can last longer. Precipitation intensity also roughly matches precipitation values observed over tropical islands (Qian et al., 2013). These features show that the simulated diurnal cycle is realistic.

The distance of maximum offshore propagation varies significantly during the simulation, with a significant number of cases where convection propagates far away, up to 600 km from the coast, or stays close to the island. The instances of long propagation show that convection generally propagates further away every day

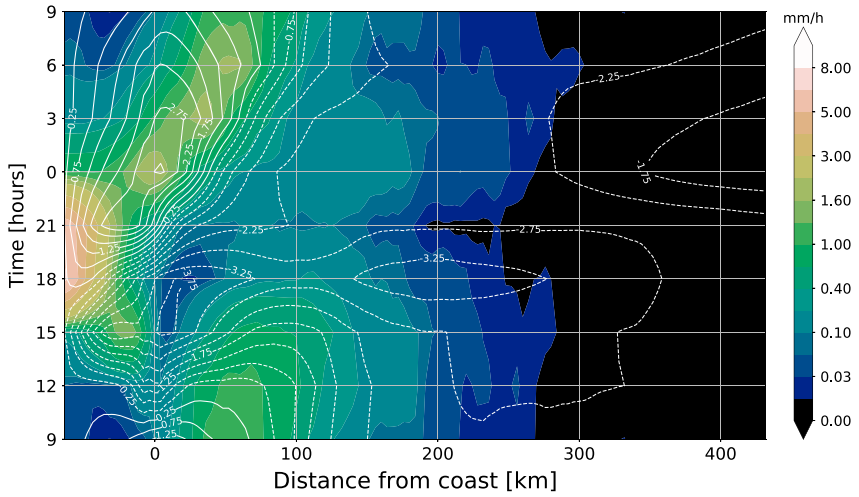

Figure 2. Diurnal composite of precipitation at the surface (shading) and wind at 75 m (contours) over 200 days. The composite considers both sides of the island and is built so that the left of the figure is the center of the island. All distances are relative to the coast (0 mark). Positive wind anomalies are represented by plain white lines and negative wind anomalies by dashed white lines.

until it reaches a maximum that can be 400–500 km from the coast. The rapid onset and propagation of these events generally occurs a few days after a period of short propagation. The transition to short-propagation days is usually very fast too.

The large day-to-day variability in the propagation makes it difficult to pinpoint specific signals in the diurnal Hovmoller of precipitation and wind (Figure 2). We can nevertheless distinguish several features. Because convection is always mostly localized over the island and its surrounding oceans, an overturning circulation develops over the whole domain. The lower branch of this large-scale circulation is associated with low-level winds converging toward the island. Thus, even though no large-scale constant wind is imposed, there is always a large-scale wind far from the coast because of this overturning circulation. In the rest of the paper, large-scale winds refer to the winds associated with this large-scale overturning circulation.

The large-scale wind further than 150 km from the coast is similar all day long and is directed onshore with a speed of 2–3 m/s, as a result of the circulation responding to the enhanced convection over the island. At the coast, the sea breeze is clearly visible. The wind blows onshore from 10:00 to 20:00 with a maximum of 3.25 m/s between 15:00 and 18:00. The reinforcement of this onshore wind is triggered by the strong warming over the island, visible at 12:00 and 15:00 in Figure 3. This figure also shows that the sea breeze circulation extends up to 100 km from the coast.

The maximum of precipitation moving at 3 m/s from the coast at night is associated with a strong offshore wind and large negative temperature anomaly that stay confined in the first 500 m of the boundary layer. Both propagate together until the next morning. The propagation speed of this maximum slightly slows down after reaching 50 km from the coast when the wind decreases (Figure 2). The region of precipitation widens and the edge of the convective envelope propagates faster at 8 m/s and generally reaches 100 km from the coast at 23:00, before abruptly slowing down.

The last noticeable feature in Figure 2 is the local maximum of precipitation around 130 km from the coast at midnight. This maximum appears stationary and could be initiated by a much faster wave which triggers convection as far as 250 km from the coast. Precipitation persists for a few hours until the slower offshore propagation from the island reaches the same area and may help maintain favorable conditions for the land breeze front to propagate.

Figure 3 enables us to identify several temperature perturbations propagating from the coast. The first one is associated with the diurnal heating of the troposphere over the island. The warm phase of this perturbation propagates at 30 m/s around 3–4 km of altitude in the early afternoon. It is followed by a cold phase propagating at a similar speed. A slower positive temperature anomaly is visible between 1 and 2 km from 15:00 to 03:00, though it is difficult to estimate its speed due to its dispersion and low amplitude.

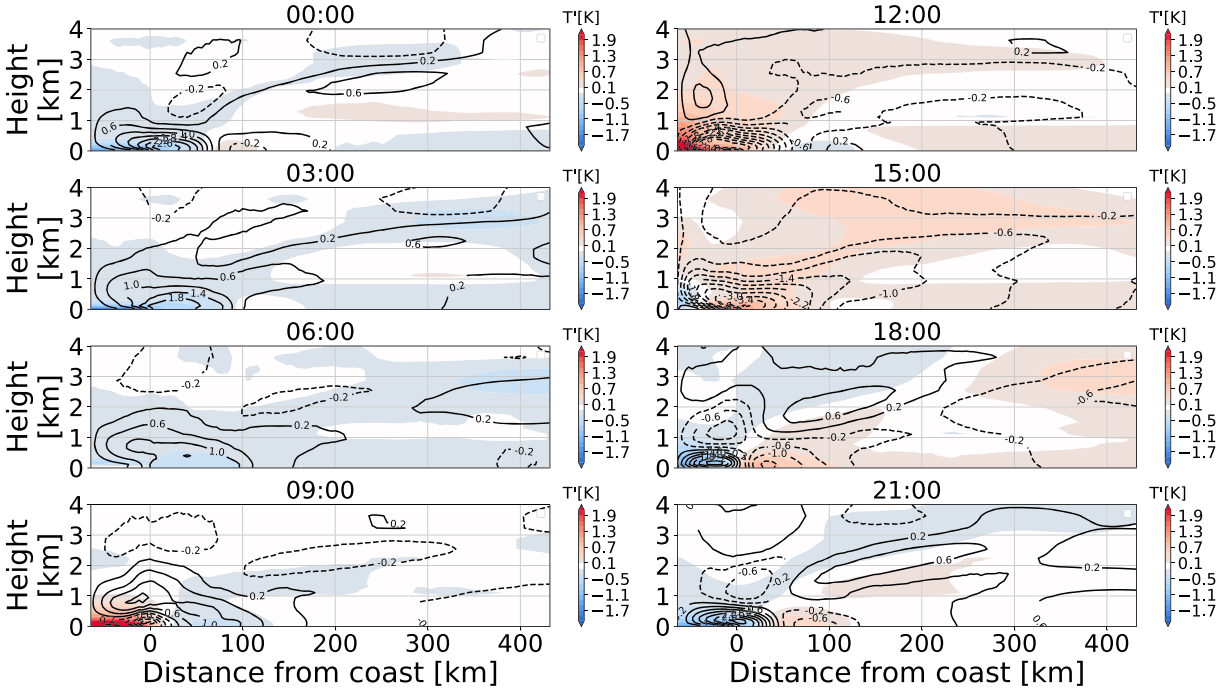

Figure 3. Temperature (shading) and wind (contours) anomalies profiles every 3 hr averaged over 200 days. The center of the island is on the left. The anomalies are calculated relative to daily average.

4. Composites by Distance of Propagation

As emphasized by Figures 2 and 3, it is difficult to clearly identify processes in the all-day composite because of the large day-to-day variability in the distance of propagation. This variability stems either from differences in offshore conditions or from different physical mechanisms at play. In order to clarify these differences, we composite the days based on the maximum distance of propagation. A threshold of 0.33 mm/hr is used to detect the maximum distance. We choose this threshold as it gives a smoother distribution of propagation distance and clearer composites, but the results are not significantly different with alternative thresholds (0.11, 0.17, 0.67, and 1 mm/hr). The maximum distance is defined as the point furthest from the

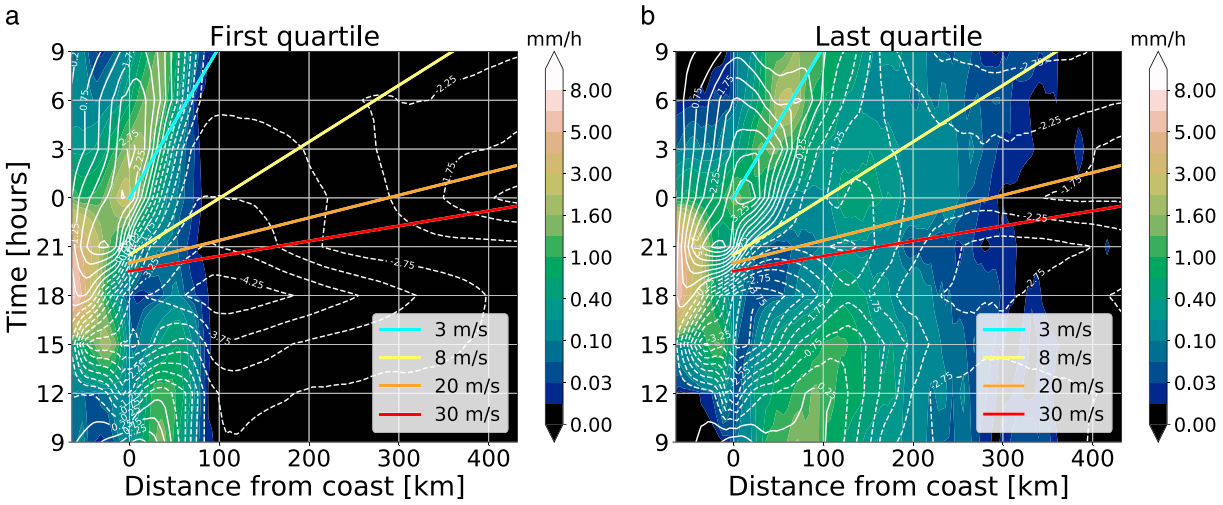

Figure 4. Diurnal composite of surface precipitation (shading) and wind at 75 m (contours, plain line for positive, dashed line for negative) averaged over the days with (a) the shortest propagation and (b) the longest propagation. The light blue, yellow, orange, and red lines indicate speeds of 3, 8, 20, and 30 m/s, respectively.

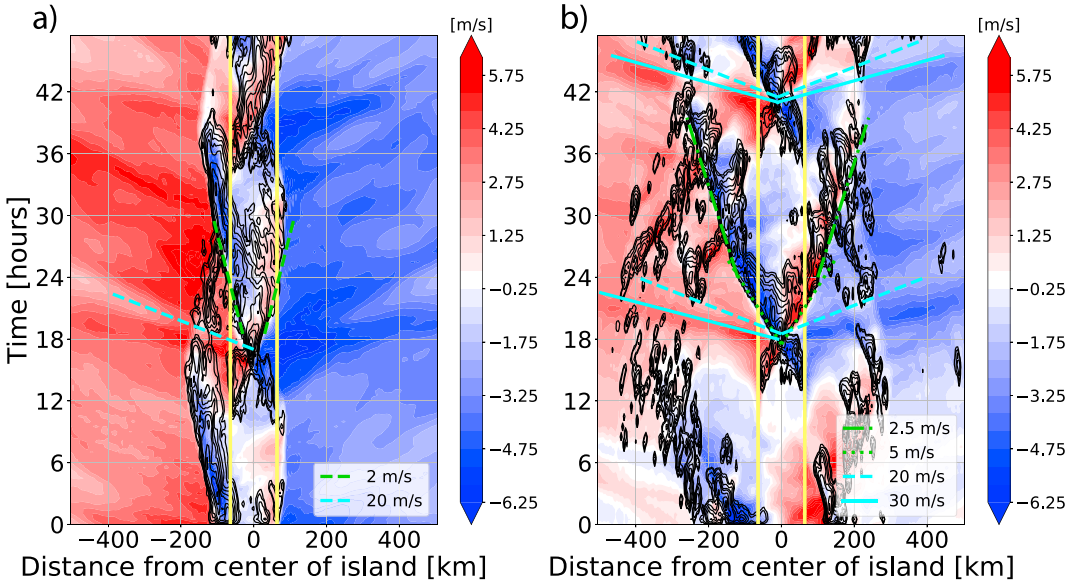

Figure 5. Hovmoller plot of the wind at 100 m (colors) and precipitation (black contours) for (a) days 60–61 and (b) days 194–195 in Figure 1. The dashed and plain light blue lines indicate speeds of 20 and 30 m/s, respectively. The dashed, semidashed, and dotted green lines indicate speeds of 2, 2.5, and 5 m/s, respectively.

coast where precipitation exceeds the threshold at least once in 24 hr. Both sides of the island are considered independent to increase the sampling size.

The mean distance of maximum propagation is 141 km from the coast (median value is 118 km). The 1st, 25th, 75th, and 99th percentiles are at 10, 81, 186, and 430 km, respectively. In order to investigate the differences between short and long propagation, we contrast the composites of the first and last quartiles. In these composites, diurnal patterns of precipitation and surface wind differ very significantly from each other (Figure 4) and from the all-days composite (Figure 2). The precipitation signal far offshore around midnight in Figure 2 is absent from the short-propagation days and goes as far as 350 km from the coast for the longest propagation. For the long propagation, convective triggering propagates away from the island evening precipitation maximum at a speed of 30 m/s (0.3-mm/hr contour aligns with red line in Figure 4b) with an

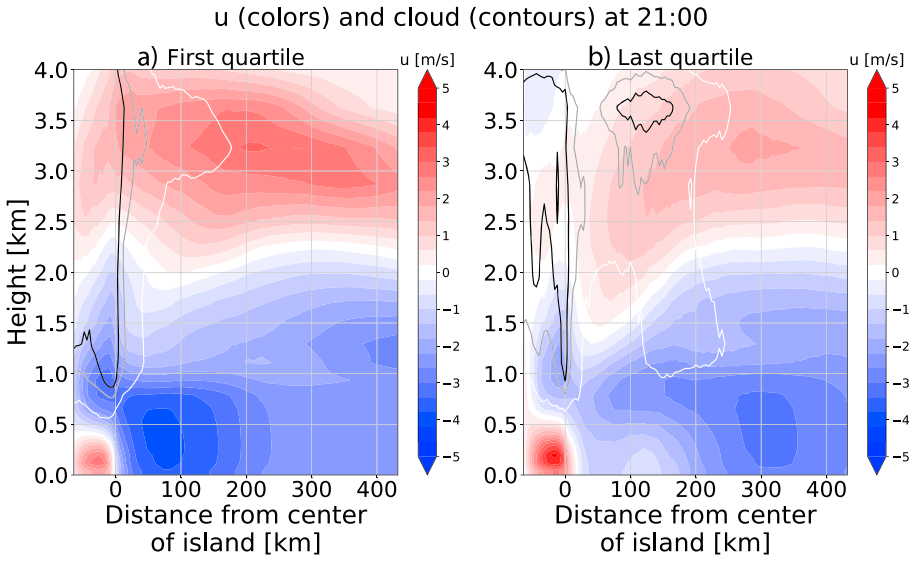

Figure 6. Wind (shading) and cloud (contours at 10^{-5}, 10^{-4}, and 10^{-3} g/kg) profiles at 21:00 averaged over the first days of (a) short propagation and (b) long propagation. The center of the island is on the left.

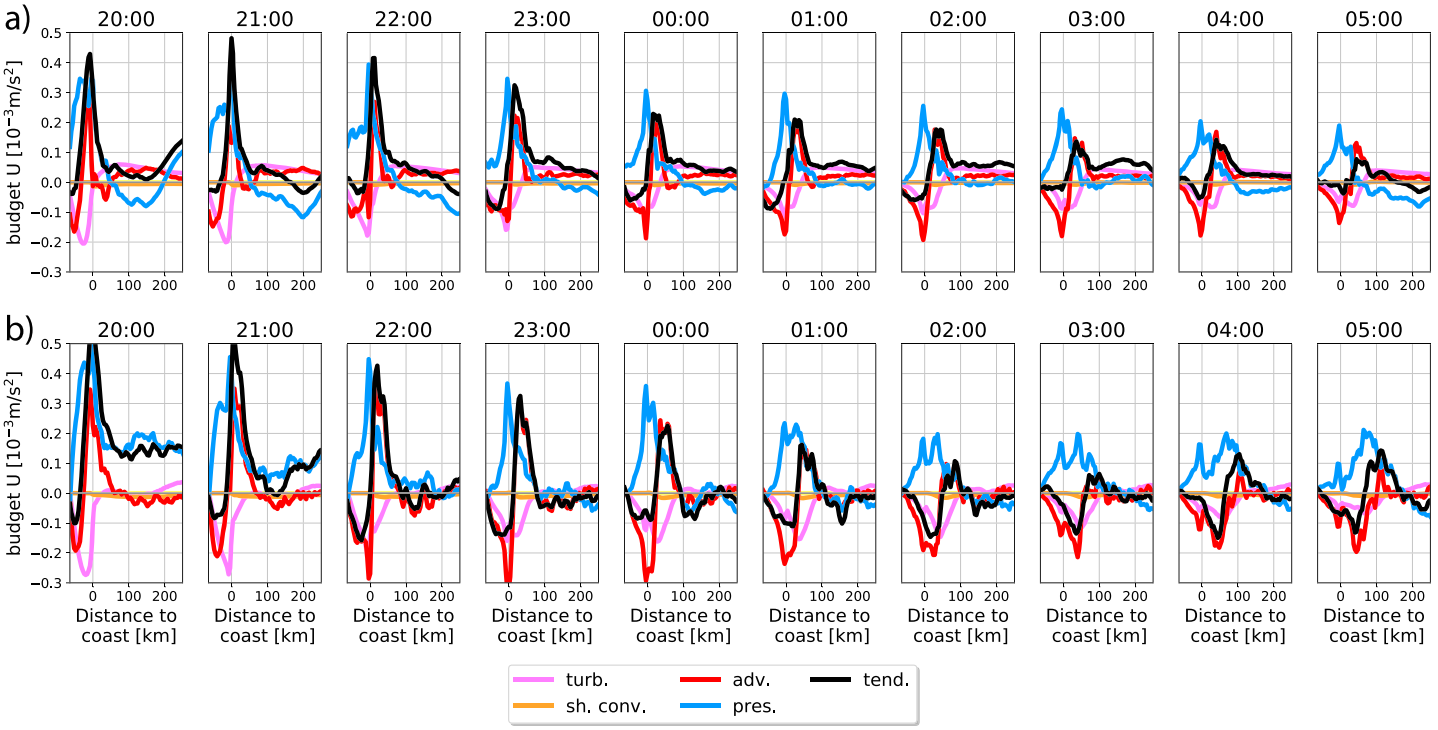

Figure 7. Transect of the 1-hr composites of the zonal wind budget between 20:00 and 07:00 averaged between the surface and 500 m for (a) the shortest propagation and (b) the longest propagation. The center of the island is on the left. The total tendency, pressure, advection, shallow convection, and turbulence components are represented by the black, blue, red, orange, and pink lines.

intensification of precipitation along a 20-m/s line (orange line). The far offshore, midnight precipitation maximum coincides with a wave propagating between 8 and 10 m/s from the island. These features are clearly highlighted when we look at days representative of both types of propagation (Figure 5). Convection is first triggered far from the coast either along the 30-m/s line or the 20-m/s line. This offshore triggering only occurs in regions where convection was present the day before. Then, it is generally advected toward the island by the large-scale wind and merges with the land breeze front propagating from the island at night. Because of the convergence convection generates at its base, offshore convection significantly decreases the low-level onshore wind all day long. This does not considerably change the maximum strength of the sea breeze (0.5-m/s decrease) but decreases the wind by 2 to 3 m/s within the first 100 km at 21:00 (Figure 6). This decreased onshore wind probably accelerates the propagation speed of both the convective envelope and the precipitation maximum. In the long propagation cases, the maximum propagates on average at 3 m/s, almost 2 m/s faster than for the short propagation (Figure 4). The same is true for the first precipitation envelope (10 versus 8 m/s). Note that these values can vary significantly from 1 day to another or for the same night, as illustrated by Figure 5. This figure also illustrates that the first precipitation envelope along the 8–10 m/s is in fact an average of individual offshore convective systems moving onshore rather than another independent front propagating from the coast.

5. Land Breeze Front

In order to investigate the physical mechanisms responsible for the nighttime offshore propagation of convection, we look at the budget of momentum integrated between the surface and 500 m, which is the top of the wind anomaly propagating offshore in Figure 3. We investigate both short and long propagation composites to detect any difference in the physical mechanisms at play (Figure 7).

In both cases, the positive wind anomaly associated with the offshore wind primarily originates from the advection term, which confirms that the propagation is due to frontal dynamics. The pressure gradient term also contributes significantly at the beginning of the propagation and then follows the advective tendency. It stays positive at night over land because the land becomes cooler than the sea. The turbulence distributes

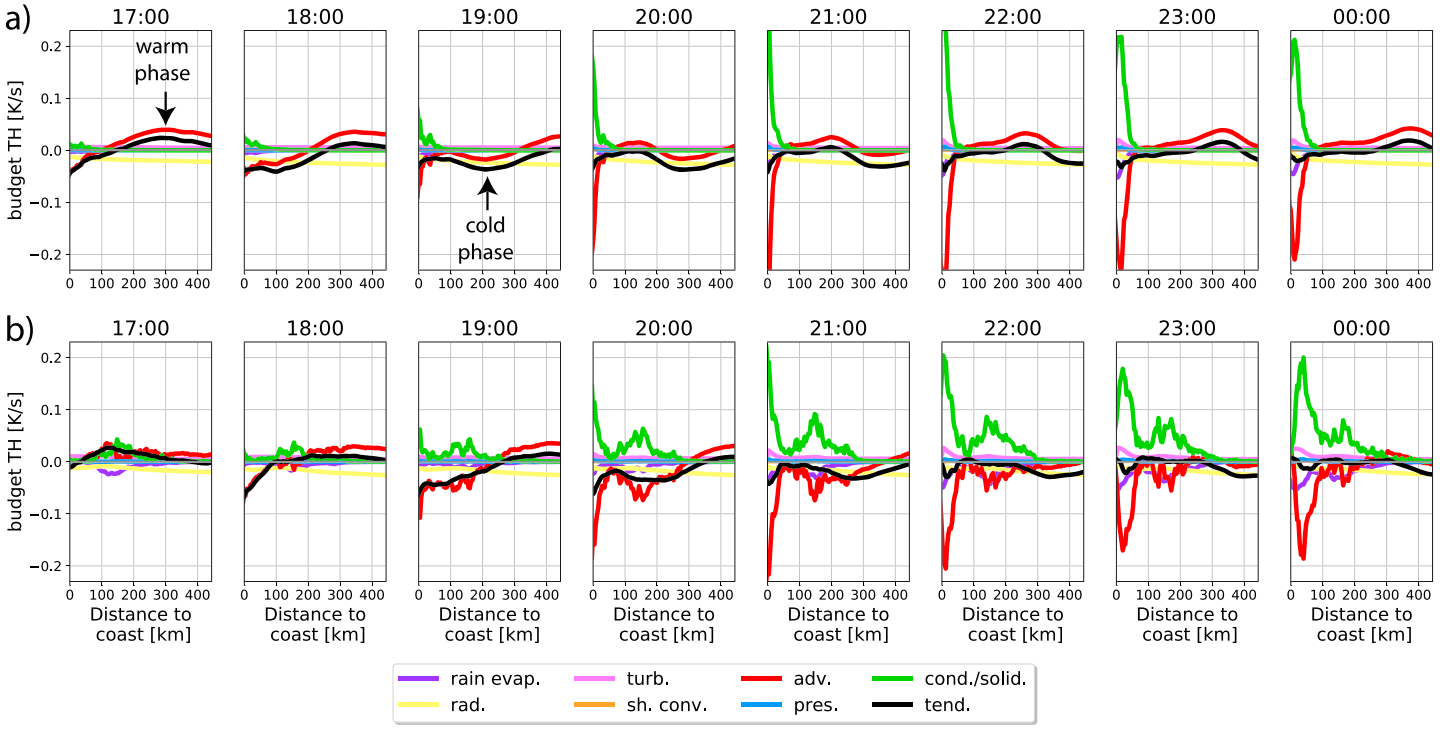

Figure 8. Same as Figure 7 for the temperature budget at 4 km. The total tendency, pressure, advection, shallow convection, turbulence, radiation, rain evaporation, and phase changes components are represented by the black, blue, red, orange, pink, yellow, purple, and green lines. Note that the abscissa starts at the coast and goes up to 400 km to be able to show the gravity wave, compared to 250 km for Figure 7.

surface friction throughout the boundary layer and as a result its tendency opposes the pressure tendency over the island and the positive advective tendency along the propagation.

The positive peak of the advection term moves at 3.5 m/s between 20:00 and 4:00 for the long propagation, much faster than for the short propagation (1.3 m/s). A look at the temperature budget integrated over the same height shows that the cold anomaly propagates at the same speed and is also controlled by the advection (not shown). Since these speeds correspond to the propagation speed of the maximum of precipitation in Figure 4 as well as differences observed between the two examples in Figure 5, we can conclude that this maximum of precipitation is the signature of the land breeze front: intense convergence at the front creates ascent and convection. It also explains why the wind pattern closely matches the maximum of precipitation rather than following the development of convection. Because the propagation speed of the land breeze is the same as the absolute wind, the difference in propagation speed of the land breeze between the short and long propagation is independent of the strength of their advection term.

Another difference between the two composites is the offshore wind reinforcement (positive tendency term) by the pressure term at 4:00 for the long propagation. This happens when the land breeze meets the offshore convection triggered 100 km away from the coast earlier in the evening and advected toward the land breeze front shown in Figure 5b. Their meeting seems to reinforce convection and may explain why convection continues to move offshore while it hovers over a constant location when this convective pattern is absent. On the other hand, while offshore-triggered convection decreases the large-scale wind on the land breeze side because of the convergence at its base, this wind is generally amplified on the other side. This may explain why the land breeze slows down around 03:00 in the other composites (Figures 2 and 4a), when it crosses these onshore-moving convective systems.

The onset of the sea breeze occurs, while the land breeze still propagates offshore. It slowly erodes the land breeze. As a result, the land breeze usually does not propagate a lot more than 24 hr. In the most favorable cases where the land breeze front moves at 4 m/s, this allows convection to reach 350 km offshore in 24 hr, which is roughly the maximum distances observed in Figure 1.

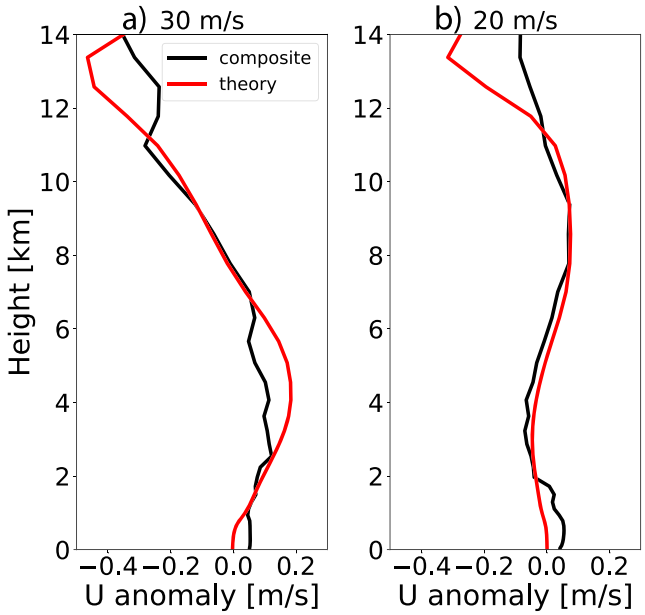

Figure 9. Wind anomaly profiles of the theoretical vertical modes (red) and composited over wind anomalies propagating at the same speed in the simulation (black) for (a) the 30-m/s gravity wave and (b) the 20-m/s gravity wave.

6. Offshore Triggering of Convection by Gravity Waves

This pattern of convection triggered more than 100 km away from the coast early in the evening appears crucial to determine the extent of the land breeze propagation. Now, we investigate what triggers this convection in the case of long propagation and compare it with the short propagation.

Figures 4 and 5 show that the triggering occurs along both 30- and 20-m/s lines propagating from the island evening precipitation maximum. The 30 m/s is also the propagation speed of the warm temperature anomaly emanating from the island in the afternoon at 4 km (see Figure 3). Since this anomaly originates from the tropospheric heating over the island during the day, we expect to find a gravity wave signature in the temperature budget at 4 km (Figure 8). This figure shows that the temperature anomaly over the sea is controlled almost exclusively by advection. The gravity wave is also triggered 1 hr earlier for the short-propagation cases. The positive tendency due to condensation indicates convection. For the long propagation, this happens as soon as the cold phase arrives, while for the short propagation, the cold anomaly is not sufficient to trigger convection. In both cases, once convection occurs, upward motion also develops and the temperature tendency due to vertical advection opposes the condensational warming. The cold phase of the gravity wave originally propagates at 30 m/s between 17:00 and 19:00 before slowing down slightly to 20 m/s between 19:00 and 22:00. This shows that the 30- and 20-m/s waves both contribute to the cold phase responsible for convection triggering.

In order to confirm that both waves are gravity waves generated by convection, we calculate the wind anomaly profile associated with these waves and compare it with the vertical modes calculated from the anelastic equations with the density and potential temperature profiles at equilibrium, under the hydrostatic approximation. For our simulation, the profile is composited along 30- and 20-m/s perturbations detected in the 4 days shown in Figure 5, that is, along the light blue lines in that figure. We include other wave signatures in the composite even if they do not trigger convection. A Fourier transform is used to filter out the first six harmonics of the diurnal cycle and keep only short-scale perturbations.

To investigate these modes, we perform the theoretical calculation of the normal modes of internal gravity waves using the average density profile with boundary conditions of zero vertical wind at the surface and at the top, following Gill (1982). The theoretical calculation of the vertical structures of the hydrostatic gravity waves produces two modes propagating at 30 and 20 m/s (red lines in Figures 9a and 9b, respectively). The 30-m/s mode has a first baroclinic vertical structure, while the 20 m/s is associated with a second baroclinic

vertical structure. The first baroclinic mode results from the midtropospheric warming associated with convection over the island in the afternoon, while the second baroclinic mode comes from its transition toward a more stratiform convection in the early evening. The profiles composited along perturbations propagating at the same respective speed (black lines) are very similar to the theoretical vertical profiles and confirm that gravity waves associated with these two vertical profiles of convective heating are responsible for the rapid triggering of offshore convection, either directly or by making the environment more favorable for convection, which is then triggered by the propagating land breeze front.

Higher-order baroclinic modes can also be detected and contribute to the triggering of offshore convection as well. For example, in Figure 8a, the warm phase propagating from 150 km at 20:00 to 375 km at 00:00 is associated with the third baroclinic mode propagating at 15 m/s. Slower, higher-order gravity wave modes (propagating at 12, 10, and 8 m/s for the fourth, fifth and sixth baroclinic modes, respectively) are also visible in Figure 5b and explain the broad convective envelope preceding the land breeze front in Figure 4. But all these higher-order modes are less systematic than the first and second baroclinic modes that dominate the wind and temperature signals.

In Figure 8, the warm and cold anomalies have the same amplitude in both cases, hinting at an environmental control on the triggering of convection. We hypothesize that the land breeze, when it propagates beyond 100 km offshore as in Figure 4b, creates an environment favorable for convection. When the cold phase of the fast gravity wave reaches this distance on the next day, convection develops. The progressive increase in propagation distance in several consecutive days supports this hypothesis (Figure 1).

7. Large-Scale Versus Local Control of the Distance of Propagation

While a moistening by previous propagating disturbances or a gravity wave can favor convection triggering far from the coast, large-scale processes can also contribute to favoring or inhibiting convection away from the coast. In order to investigate what role the land breeze and the large-scale environment have in controlling the distance of propagation, we consider only the first day with long propagation following a period of short propagation and, conversely, the first day with short propagation following a period of long propagation. Because these events generally recur with a 20-day period (Figure 1), if two separate days are identified as the first of a short (or long) propagation period within 12 consecutive days, we only keep the first one in order to avoid including an environment favorable for short (or long) propagation in the composite. Our results are insensitive to the value of this threshold within the interval 6–18 days.

Isolating the first day of short or long propagation allows us to look at the offshore environment when such propagation occurs, as well as in the days preceding it, before the propagation itself modifies this environment. The daily-averaged temperature and humidity anomalies in the days leading to short propagation highlight a warm and dry anomaly approaching the coast in the lower free troposphere (first row in Figure 10). This dry anomaly is advected by the large-scale overturning wind, as shown by the humidity budget for the first short propagation (Figure 11). The absence of increased subsidence over the region indicates that the advection is horizontal (not shown). Because it sits on top of the boundary layer, this anomaly stabilizes the lower troposphere and inhibits convection, leading to short propagation.

For long propagation, we notice a gradual cooling and humidification of a previously dry region at the top of the boundary layer between 150 and 200 km (second row in Figure 10), which corresponds to a deepening of the boundary layer. The humidity budget on the day of first long propagation and 2 days before shows that shallow convection, turbulence, and advection humidify the top of the boundary layer between 100 and 200 km prior to long propagation (Figure 12). On the first day of long propagation, shallow convection and turbulence still act as precursors for the humidification. Advection contributes around the maximum distance of propagation (between 180 and 200 km). This advection is most likely vertical since convection is occurring there and causing ascent.

Thus, even though the large-scale environment and more specifically the conditions at the top of the boundary layer control the maximum distance of offshore propagation, the importance of this control versus the local processes differs in both cases. The horizontal advection of a dry and warm anomaly at the top of the boundary layer forces convection to stay increasingly closer to the coast and emphasizes the very strong control of the short-propagation cases by the large-scale environment. This large convection-inhibiting anomaly is progressively damped by the land breeze front propagating increasingly further from the island at night,

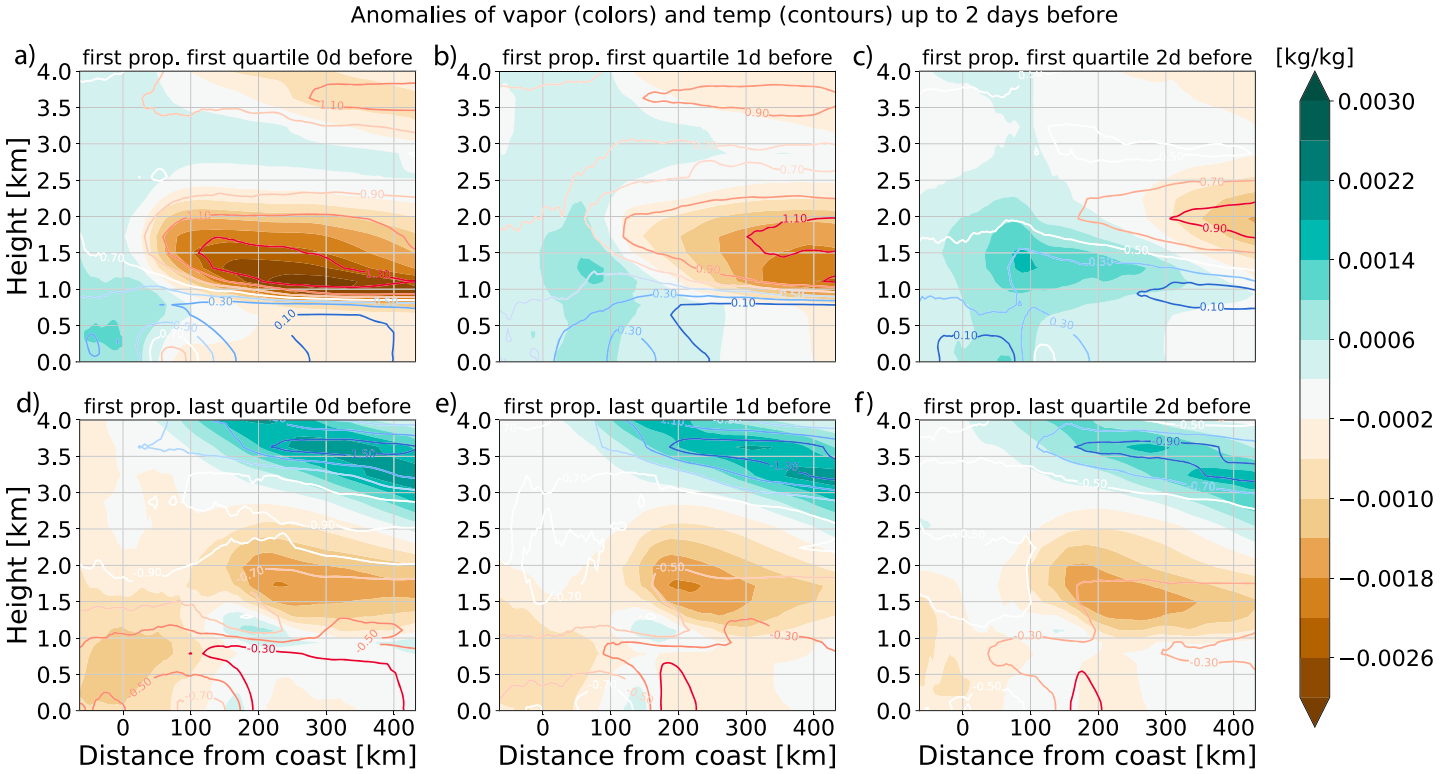

Figure 10. (first row) Daily mean profiles of humidity (shading) and temperature (contours) anomalies for (a) the first day of short propagation, (b) 1 day before, and (c) 2 days before. (second row) same for (d) the first day of long propagation, (e) 1 day before, and (f) 2 days before. The anomalies are calculated relative to daily average for the 200 days at each point in the *x* direction.

which highlights the role played by local processes such as shallow convection prior to the first long propagation. Once the boundary layer is sufficiently deep, the cold phase of the fast gravity waves forced by heating over the island during the afternoon triggers convection far from the coast. This convection is advected toward the land breeze front. It also decreases the wind from the lower branch of the large-scale overturning circulation and favors a faster propagation of the land breeze front (Figure 6). Once the land breeze merges with the convective systems triggered by the earlier gravity wave, it gets reinforced and propagates further.

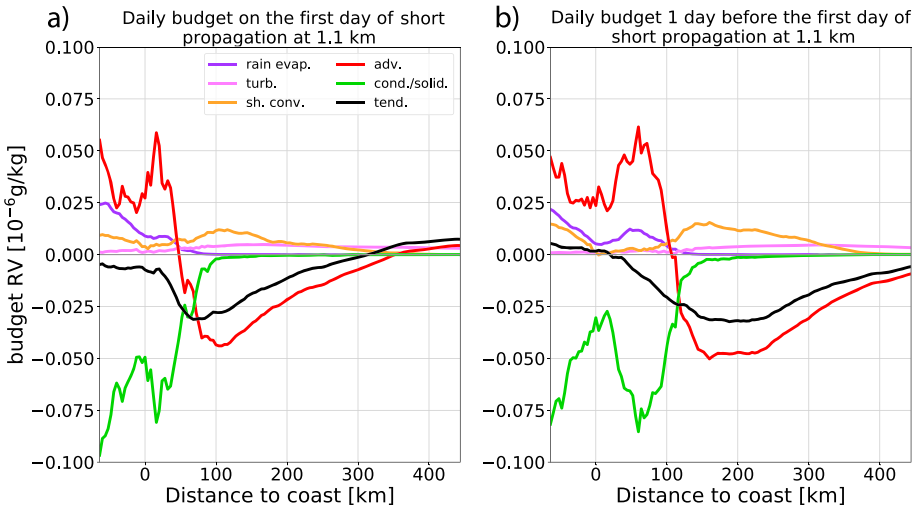

Figure 11. Transect of the daily budget of humidity at 1.1 km for (a) the first days of short propagation and (b) 1 day before.

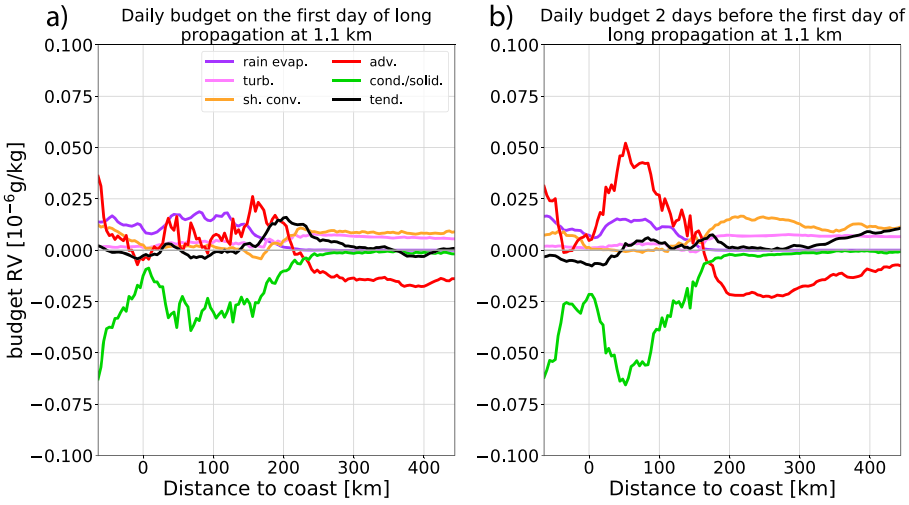

Figure 12. Same as Figure 11 for (a) the first days of long propagation and (b) 2 days before.

This creates favorable conditions for convection to get triggered even further away the next day and explains why convection can very quickly propagate more than 300 km away from the coast.

8. Discussion and Conclusions

In this study, we investigate the physical mechanisms controlling the offshore propagation of convection over an idealized rectangular island using the nonhydrostatic atmospheric model Meso-NH in RCE configuration. We focus on a simulation without any topography. The large-scale wind is set to zero.

The diurnal cycle of convection over the island is controlled by a land-sea breeze circulation. Precipitation realistically peaks in the late afternoon-early evening over the island before propagating offshore at night. The propagation shares many similarities with other studies:

- A land breeze front propagates away from the coast at night. This land breeze is evidenced by advection controlling the wind and temperature budgets integrated over the first 500 m of the boundary layer. The land breeze front propagates at an average speed of 3–4 m/s, which is consistent with the propagation speed of the precipitation maximum found in observations (Mori et al., 2011; Yokoi et al., 2017) and other high-resolution modeling studies (Hassim et al., 2016; Love et al., 2011; Vincent & Lane, 2016). This speed depends on the large-scale wind speed, itself mostly modulated by the presence of convection further offshore.
- The offshore rainfall onset propagating from the coast, in which the land breeze propagates, moves at 8–10 m/s. It corresponds to speeds estimated in observations near Sumatra (Mori et al., 2004; Yokoi et al., 2017). But even though high-order gravity wave modes propagating at these speeds can trigger convection prior to the land breeze front, they do not usually trigger convection along a line that would define the envelope visible in the composite. In our model, these modes correspond to the third to sixth baroclinic modes and propagate at 15, 12, 10, and 8 m/s, respectively. In reality, these modes either trigger new convection or reinforce convection triggered earlier by a faster gravity wave. This new convection is usually advected by the wind from the lower branch of the large-scale overturning circulation toward the land breeze front. Thus, the rainfall onset in the composite mainly results from averaging of all these small convective systems.
- The heating over the island in the afternoon and early evening triggers gravity waves moving at 30 and 20 m/s every day. These waves are evidenced by the temperature budget at 4 km and have a similar vertical structures to the first and second baroclinic vertical modes. The cold phase of these gravity waves trigger convection far from the coast (more than 100 km away) when the offshore atmospheric conditions are favorable. The fastest gravity wave is quite similar to the gravity wave found in Mapes et al. (2003) or forced in the 4-km resolution of Love et al. (2011), even though they found a slightly faster propagation in the latter.

The large-scale variability, in particular of temperature and humidity at the top of the boundary layer, plays a crucial role in controlling how far offshore convection propagates. Short propagation takes place when

a warm and dry anomaly is advected above the boundary layer. This anomaly stabilizes the atmosphere and prevents the onset of convection. Long propagation is possible after shallow convection and vertical advection gradually deepen the boundary layer and reduce convective inhibition. In this case, the gravity wave is able to trigger convection far from the coast. This convection is advected toward the land breeze front, but because of the convergence it generates at its base, it shelters the breeze front from the large-scale wind, allowing a faster propagation of the land breeze. Once the land breeze and the offshore convection merge, convection is reinforced and propagates further away from the coast but at a slower speed. It also creates favorable conditions for future convection even further away and explains how convection can rapidly transition from short propagation to propagation as far as 400 km from the coast.

Overall, this study confirms observational results and previous modeling work. It shows how important the large-scale environment is for the offshore propagation of convection. But so far, the few observational studies looking at offshore propagation of convection did so over short-term campaigns. Now that algorithms able to track offshore-propagating systems originating from islands exist, it might be possible to assess more precisely the role that large-scale environment plays in those events.

In addition to the large-scale environment, boundary layer processes are also crucial since they modulate the environment at the top of the boundary layer and oppose the effect of the large-scale environment as they do for the first days of long propagation. Better parameterizations of these processes might improve the performance of models with coarser resolution around the islands.

Considering how topography is known to affect the propagation of the land breeze via mountain-valley breeze (Qian, 2008; Vincent & Lane, 2016) and the generation of gravity wave (Mapes et al., 2003), our next step is to explore how topography modulates the offshore propagation of convection in a similar framework. This is done in part II of this work (Coppin & Bellon, 2019) which explores the impact of two different mountain shapes: one with a central ridge and one with a peak and a pass.

Acknowledgments
We thank two anonymous reviewers for their helpful comments. We acknowledge the financial support of the Glavish Postdoctoral Fellowship and the Buckley-Glavish Lectureship, as well as support from the University of Auckland. We also wish to acknowledge the use of New Zealand eScience Infrastructure (NeSI) high-performance computing facilities and consulting support as part of this research. New Zealand's national facilities are provided by NeSI and funded jointly by NeSI's collaborator institutions and through the Ministry of Business, Innovation and Employment's Research Infrastructure programme (https://www.nesi.org.nz). We also thank MesoNH team at CNRM and LA, Toulouse, France: Christine Lac, Juan Escobar, Gaelle Gautier, Philippe Vautelet, as well as Stéphanie Faroux, Jean-Pierre Pinty, and Jean-Pierre Chaboureau. Data used in this study can be found online (https://www.dropbox.com/sh/gyt8uruv2f36cer/AAB0uE_9qeyOPqaRnBg5Gfv_a?dl=0).

References

Bechtold, P., Semane, N., Lopez, P., Chaboureau, J. P., Beljaars, A., & Bormann, N. (2014). Representing equilibrium and nonequilibrium convection in large-scale models. *Journal of the Atmospheric Sciences*, *71*(2), 734–753. https://doi.org/10.1175/JAS-D-13-0163.1

Coppin, D., & Bellon, G. (2019). Physical mechanisms controlling the offshore propagation of convection in the tropics: 2. Influence of topography. *Journal of Advances in Modeling Earth Systems*, *11*. https://doi.org/10.1029/2019MS001794

Cronin, T. W., Emanuel, K. A., & Molnar, P. (2015). Island precipitation enhancement and the diurnal cycle in radiative-convective equilibrium. *Quarterly Journal of the Royal Meteorological Society*, *141*, 1017–1034. https://doi.org/10.1002/qj.2443

Cuxart, J., Bougeault, P., & Redelsperger, J.-L. (2000). A turbulence scheme allowing for mesoscale and large-eddy simulations. *Quarterly Journal of the Royal Meteorological Society2*, *126*, 1–30. https://doi.org/10.1256/qj.03.133

Cuxart, J., Jiménez, M. A., Prtenjak Telišman, M., & Grisogono, B. (2014). Study of a sea-breeze case through momentum, temperature, and turbulence budgets. *Journal of Applied Meteorology and Climatology*, *53*(11), 2589–2609. https://doi.org/10.1175/JAMC-D-14-0007.1

Emanuel, K. A., Wing, A. A., & Vincent, E. M. (2014). Radiative-convective instability. *Journal of Advances in Modeling Earth Systems*, *6*, 75–90. https://doi.org/10.1002/2013MS000270

Fouquart, Y., & Bonnel, B. (1980). Computations of solar heating of the Earth's atmosphere: A new parameterization. *Beitrage zur Physik der Atmosphare*, *53*, 35–62.

Gill, A. E. (1982). *Atmosphere-ocean dynamics Edited by* W. L. Donn. San Diego: Academic Press.

Hassim, M. E. E., Lane, T. P., & Grabowski, W. W. (2016). The diurnal cycle of rainfall over New Guinea in convection-permitting WRF simulations. *Atmospheric Chemistry and Physics*, *16*(1), 161–175. https://doi.org/10.5194/acp-16-161-2016

Ichikawa, H., & Yasunari, T. (2007). Propagating diurnal disturbances embedded in the Madden-Julian Oscillation. *Geophysical Research Letters*, *34*, L18811. https://doi.org/10.1029/2007GL030480

Ichikawa, H., & Yasunari, T. (2008). Intraseasonal variability in diurnal rainfall over New Guinea and the surrounding oceans during Austral summer. *Journal of Climate*, *21*, 2852–2868. https://doi.org/10.1175/2007JCLI1784.1

Lac, C., Masson, V., Aouizerats, B., Augros, C., Aumond, P., Caumont, O., et al. (2018). Overview of the Meso-NH model version 5.4 and its applications. *Geoscientific Model Development*, *11*, 1929–1969.

Lafore, J. P., Stein, J., Asencio, N., Bougeault, P., Ducrocq, V., Duron, J., et al. (1998). The Meso-NH atmospheric simulation system. Part I: Adiabatic formulation and control simulations. *Annales Geophysicae*, *16*, 90–109.

Li, Y., Jourdain, N. C., Taschetto, A. S., Gupta, A. S., Argüeso, D., Masson, S., & Cai, W. (2017). Resolution dependence of the simulated precipitation and diurnal cycle over the Maritime Continent. *Climate Dynamics*, *48*(11-12), 4009–4028. https://doi.org/10.1007/s00382-016-3317-y

Love, B. S., Matthews, A. J., & Lister, G. M. S. (2011). The diurnal cycle of precipitation over the Maritime Continent in a high-resolution atmospheric model. *Quarterly Journal of the Royal Meteorological Society*, *137*, 934–947. https://doi.org/10.1002/qj.809

Mapes, B. E., & Houze, R. A. (1993). Cloud clusters and superclusters over the oceanic warm pool. *Monthly Weather Review*, *121*, 1398–1415.

Mapes, B. E., Warner, T. T., & Xu, M. (2003). Diurnal patterns of rainfall in Northwestern South America. Part III: Diurnal gravity waves and nocturnal convection offshore. *Monthly Weather Review*, *131*, 830–844.

Mapes, B. E., Warner, T. T., Xu, M., & Negri, A. J. (2003). Diurnal patterns of rainfall in Northwestern South America. Part I: Observations and context. *Monthly Weather Review*, *131*(5), 799–812. Retrieved from https://doi.org/10.1175/1520-0493(2003)131<0799:DPORIN>2.0.CO;2

Masson, V., Le Moigne, P., Martin, E., Faroux, S., Alias, A., Alkama, R., et al. (2013). The SURFEXv7.2 land and ocean surface platform for coupled or offline simulation of Earth surface variables and fluxes. *Geoscientific Model Development*, *6*(4), 929–960. https://doi.org/10.5194/gmd-6-929-2013

Morcrette, J.-J. (1991). Radiation and cloud radiative properties in the European Centre for Medium Range Weather Forecasts forecasting system. *Journal of Geophysical Research*, *96*(D5), 9121–9132. Retrieved from https://doi.org/10.1029/89JD01597

Morcrette, J. J. (2002). The surface downward longwave radiation in the ECMWF forecast system. *Journal of Climate*, *15*(14), 1875–1892. https://doi.org/10.1175/1520-0442(2002)015<1875:TSDLRI>2.0.CO;2

Mori, S., Hamada, J.-I., Sakurai, N., Fudeyasu, H., Kawashima, M., Hashiguchi, H., et al. (2011). Convective systems developed along the coastline of Sumatera Island, Indonesia, observed with an X-band Doppler radar during the HARIMAU2006 campaign. *Journal of the Meteorological Society of Japan*, *89A*, 61–81. https://doi.org/10.2151/jmsj.2011-a04

Mori, S., Hamada, J. I., Tauhid, Y. I., & Yamanaka, M. D. (2004). Diurnal land-sea rainfall peak migration over Sumatra Island, Indonesian Maritime Continent, observed by TRMM satellite and intensive rawinsonde soundings. *Monthaly Weather Review*, *132*, 2021–2039.

Neale, R., & Slingo, J. (2003). The Maritime Continent and its role in the global climate: A GCM study. *Journal of Climate*, *16*(5), 834–848. https://doi.org/10.1175/1520-0442(2003)016<0834:TMCAIR>2.0.CO;2

Nesbitt, S. W., & Zipser, E. J. (2003). The diurnal cycle of rainfall and convective intensity according to three years of TRMM measurements. *Journal of Climate*, *16*, 1456–1475. https://doi.org/10.1175/1520-0442-16.10.1456

Noilhan, J., & Planton, S. (1989). A simple parameterization of land surface processes for meteorological models. *Monthly Weather Review*, *117*, 536–549.

Peatman, S. C., Matthews, A. J., & Stevens, D. P. (2015). Propagation of the Madden–Julian Oscillation and scale interaction with the diurnal cycle in a high-resolution GCM. *Climate Dynamics*, *45*, 2901–2918. https://doi.org/10.1007/s00382-015-2513-5

Pergaud, J., Masson, V., Malardel, S., & Couvreux, F. (2009). A parameterization of dry thermals and shallow cumuli for mesoscale numerical weather prediction. *Boundary-Layer Meteorology*, *132*(1), 83–106. https://doi.org/10.1007/s10546-009-9388-0

Pinty, J.-P., & Jabouille, P. (1998). A mixed-phased cloud parameterization for use in a mesoscale non-hydrostatic model: Simulations of a squall line and of orographic precipitation. In *Conf. on cloud physics*, Everett, WA, pp. 217–220.

Qian, J.-H. (2008). Why precipitation is mostly concentrated over islands in the Maritime Continent. *Journal of the Atmospheric Sciences*, *65*, 1428–1441. Retrieved from https://doi.org/10.1175/2007JAS2422.1

Qian, J.-H., Robertson, A. W., & Moron, V. (2013). Diurnal cycle in different weather regimes and rainfall variability over Borneo associated with ENSO. *Journal of Climate*, *26*, 1772–1791. https://doi.org/10.1175/JCLI-D-12-00178.1

Rochetin, N., Grandpeix, J.-Y., Rio, C., & Couvreux, F. (2014). Deep convection triggering by boundary layer thermals. Part II: Stochastic triggering parameterization for the LMDZ GCM. *Journal of the Atmospheric Sciences*, *71*(2), 515–538. https://doi.org/10.1175/jas-d-12-0337.1

Saito, K., Keenan, T. D., Holland, G., & Puri, K. (2001). Numerical simulation of the diurnal evolution of tropical island convection over the Maritime Continent. *Monthly Weather Review*, *129*, 378–400. https://doi.org/10.1175/1520-0493(2001)129<0378

Sato, T., Miura, H., Satoh, M., Takayabu, Y. N., & Wang, Y. (2009). Diurnal cycle of precipitation in the tropics simulated in a global cloud-resolving model. *Journal of Climate*, *22*(18), 4809–4826. https://doi.org/10.1175/2009JCLI2890.1

Sobel, A. H., Burleyson, C. D., & Yuter, S. E. (2011). Rain on small tropical islands. *Journal of Geophysical Research*, *116*, D08102. https://doi.org/10.1029/2010JD014695

Tulich, S. N., & Mapes, B. E. (2007). Multiscale convective wave disturbances in the tropic: Insights from a. *Journal of Atmospheric Sciences*, *65*, 140–155. https://doi.org/10.1175/2007JAS2353.1

Vincent, C. L., & Lane, T. P. (2016). Evolution of the diurnal precipitation cycle with the passage of a Madden–Julian Oscillation event through the Maritime Continent. *Monthly Weather Review*, *144*, 1983–2005. https://doi.org/10.1175/MWR-D-15-0326.1

Wang, S., & Sobel, A. H. (2017). Factors controlling rain on small tropical islands: Diurnal cycle, large-scale wind speed, and topography. *Journal of the Atmospheric Sciences*, *74*(11), 3515–3532. https://doi.org/10.1175/jas-d-16-0344.1

Yang, G., & Slingo, J. (2001). The diurnal cycle in the tropics. *Monthly Weather Review*, *129*, 784–801. https://doi.org/10.1175/1520-0493(2001)129<0784:TDCITTi2.0.CO;2

Yokoi, S., Mori, S., Katsumata, M., Geng, B., Yasunaga, K., Syamsudin, F., et al. (2017). Diurnal cycle of precipitation observed in the western coastal area of Sumatra Island: Offshore preconditioning by gravity waves. *Monthly Weather Review*, *145*, 3745–3761. https://doi.org/10.1175/MWR-D-16-0468.1